

Thallium ionic conductivity of new thallium indium hafnium molybdate ceramics

Victoria G. Grossman^a, Jibzema G. Bazarova^a, Maksim S. Molokeev^{b,c}, Bair G. Bazarov^a

^a*Baikal Institute of Nature Management, Siberian Branch, Russian Academy of Sciences, Sakhyanovoy St., 6, Ulan-Ude 670047, Buryat Republic, Russia*

^b*Kirensky Institute of Physics, Federal Research Center KSC, Siberian Branch, Russian Academy of Sciences, 50 / 38 Akademgorodok, Krasnoyarsk 660036, Russia*

^c*Siberian Federal University, 82 Svobodniy Av., Krasnoyarsk 660041, Russia*
E-mail address: grossmanv@mail.ru

ABSTRACT

In the process of studying the system Tl_2MoO_4 – $In_2(MoO_4)_3$ – $Hf(MoO_4)_2$, a new thallium indium hafnium molybdate was found. The crystal structure of the molybdate $Tl_3InHf(MoO_4)_6$ was determined in the centrosymmetric space group $R\bar{3}c$ ($a = 10.63893(5) \text{ \AA}$, $c = 38.1447(3) \text{ \AA}$; $V = 3739.04(4) \text{ \AA}^3$, $Z = 6$). The structure is a framework consisting and contains alternating mixed (Hf,In) O_6 octahedra connected by MoO_4 tetrahedra. The structure is a three-dimensional framework consisting of alternating (Hf,Fe) O_6 -octahedra connected by MoO_4 -tetrahedra. Each octahedron has common vertices with tetrahedra. The atoms arranged in this way form channels extended along with the a and b axes, in which thallium atoms are located. The conductivity behavior of $Tl_3InHf(MoO_4)_6$ ceramics was studied in the temperature range from 300 K to 870 K. The conductivity of the heavy cations of thallium is activated with increasing temperature.

Keywords: Synthesis; Thallium; Molybdates; Phase diagram; DSC; Conducting material.

1. Introduction

Currently, there is great interest in inorganic compounds (in particular, molybdenum-containing [1]) which exhibit the properties of catalysts [2–4], ferroelectric, piezoelectric, photoluminescent [5], laser [6, 7], magnetic and have high ionic conductivity [8–18].

For example, the molybdates $Gd_2W_{1-x}Mo_xO_6:Eu^{3+}$ [19], $Li_3Ba_2R_3(MoO_4)_8$ ($R = Ln$ or Y) and $LiMR_2(MoO_4)_4$ ($M = K, Rb$ or Tl ; $R = Ln, Y$ or Bi) [20–22], $CaLa_2(MoO_4)_4$ [23], $NaCaLa(MoO_4)O_3:Er^{3+}, Yb^{3+}$ [24], $NaSrLa(MoO_4)O_3$ [25] are the proposed candidates for the creation of phosphors, white LEDs, and active lasers.

At the same time, for such compounds as $Na_{1-x}A_{1-x}R_{1+x}(MoO_4)_3$ ($A = Mg, Mn, Co, Ni, Zn, Cd$; $R = Al, Fe, Cr, Sc, In$), $Ag_4M_2Zr(MoO_4)_6$ ($M = Mg, Mn, Co, Zn$) ion-conducting properties were discovered [26–28].

Based on this, we decided to study the phase equilibria in ternary salt systems, where molybdates of monovalent, trivalent, and tetravalent metals were used as starting compounds. In these systems, new compounds of several compositions were identified. One of them has the composition $M_5RA(MoO_4)_6$ (where $M = K, Rb, Cs$, $R =$ lanthanide trivalent ion, $Al^{3+}, Cr^{3+}, Fe^{3+}, In^{3+}, Sc^{3+}, Y^{3+}, Bi^{3+}$, $A = Zr^{4+}$ or Hf^{4+}) [15, 29–45]. Studies of the conductivity of these compounds showed that it has an order of $10^{-3} - 10^{-4} \text{ S cm}^{-1}$.

The molybdates are the proposed candidates for the creation of phosphors, white LEDs, and active lasers [19–25].

In recent decades, ternary molybdates with the general chemical formula $A_xB_yC_z(MoO_4)_n$, containing various combinations of A, B and C cations, have been actively studied. For these compounds, the most characteristic structures of NASICON [26] and alluaudite [27]. Due to their structural features, they have high ionic conductivity ($\sigma = 10^{-3} - 10^{-2} \text{ S cm}^{-1}$). For example, $Na_{1-x}A_{1-x}R_{1+x}(MoO_4)_3$ ($A = Mg, Mn, Co, Ni, Zn, Cd$; $R = Al, Fe, Cr, Sc, In$) and $Ag_{1-x}Mg_{1-x}R_{1+x}(MoO_4)_3$ (where $R = Al$ or Sc and $0 \leq x \leq 0.5$) crystallizes in the NASICON-type structure (space group $R\bar{3}c$) [sodium (Na) Super Ionic CONductor] [28–30]. A specific feature of phases with a NASICON structure is a rhombohedral framework $\{[R_2(MoO_4)]_3^m\}_{3\infty}$ consisting of RO_6 octahedra and MoO_4 tetrahedra. $A(R)$ atoms are at threefold axes and MoO_4 groups are at twofold axes. The vacant parts of octahedral and tetrahedral voids merge into a three-dimensional network of channels, which are filled with alkali metal cations. This contributes to high ionic conductivity $\sigma = 10^{-3} - 10^{-2} \text{ S cm}^{-1}$ at about $T = 750 - 800 \text{ K}$. $K_{0.13}Na_{3.87}Mg(MoO_4)_3$ (space group $C2/c$, $\sigma = 3.8 \times 10^{-2} \text{ S cm}^{-1}$ at 853 K) crystallizes in the alluaudite-type [31]. The structure is formed by infinite chains composed of edge sharing $(Mg/Na)_2O_{10}$ dimmers, which are linked together via bridging MoO_4 tetrahedra, yielding to a three-dimensional framework enclosing two distinct types of hexagonal tunnels in which Na^+ and K^+ cations reside. $Na_{25}Cs_8R_5(MoO_4)_{24}$ ($R = In, Sc, Fe$) form a distinctive family of pseudo-orthorhombic alluaudite-related structures with the parent space group $Pbca$ [17]. Its structural features are alluaudite-like polyhedral layers composed of pairs of edge-shared $(R,Na)O_6$ and NaO_6 octahedra connected by bridging MoO_4 tetrahedra. The layers are joined together by means of interlayer MoO_4 tetrahedra, thus forming open 3D

frameworks with cavities filled with Cs⁺ and Na⁺ ions. The manner of stacking layers is somewhat different from the alluaudite type. The conductivity for Na₂₅Cs₈R₅(MoO₄)₂₄ ($R = \text{In, Sc, Fe}$) is $\sigma = 10^{-3} - 10^{-2} \text{ S cm}^{-1}$ at about $T = 700 \text{ K}$. $M_5RA(\text{MoO}_4)_6$ (where $M = \text{K, Rb, Cs}$, $R = \text{lanthanide trivalent ion, Al}^{3+}, \text{Cr}^{3+}, \text{Fe}^{3+}, \text{In}^{3+}, \text{Sc}^{3+}, \text{Y}^{3+}, \text{Bi}^{3+}$, $A = \text{Zr}^{4+}$ or Hf^{4+}) [15, 32–48] form family with the space group $R\bar{3}c$. The crystal structure of $M_5RA(\text{MoO}_4)_6$ is a three-dimensional mixed-metal framework, which is built by a regular alternation of Mo tetrahedra and two sorts of $(R,A)\text{O}_6$ octahedra, which are linked to one another via O-corner sharing. Large interstices accommodate two sorts of alkaline atoms. These M^+ polyhedra fill in variously oriented large-cross-section channels. From this, conditions for rapid ion transport can appear in this type of framework structure provided that channels are populated by appropriate cations with appropriate ionic radii. Studies of the conductivity of these compounds showed that it has an order of $10^{-3} \text{ S cm}^{-1}$.

In this regard, the idea arose to replace the alkali metal with thallium. Since the compounds $M_5RA(\text{MoO}_4)_6$ (where $M = \text{K, Rb, Cs}$, $R = \text{lanthanide trivalent ion, Al}^{3+}, \text{Cr}^{3+}, \text{Fe}^{3+}, \text{In}^{3+}, \text{Sc}^{3+}, \text{Y}^{3+}, \text{Bi}^{3+}$, $A = \text{Zr}^{4+}$ or Hf^{4+}) [15, 32–48] were obtained only with alkali metals, the idea arose to replace the alkali metal with thallium. Thallium is a rather uncommon element. The presence of a lone pair of electrons in the monovalent thallium cation can contribute to the distortion of the coordination environment, which in turn may improve the conductive properties of $M_5RA(\text{MoO}_4)_6$. As a trivalent metal, we decided to use indium. For us, the study of this class of compounds is of not only practical but also theoretical interest.

2. Experimental

2.1. Preparation of samples

The complex molybdate compositions were prepared by the solid state reaction method. Tl_2CO_3 (chemically pure, Red Chemist, Russia), In_2O_3 (chemically pure, Ural Plant of Chemical Reagents, Russia), HfO_2 (chemically pure, IGIC RAS, Russia) and MoO_3 (chemically pure, Red Chemist, Russia) were used as starting reagents. A stoichiometric mixture of In_2O_3 and MoO_3 was used for the synthesis of $\text{In}_2(\text{MoO}_4)_3$ at 673–1023 K for 50 h. To avoid losses of MoO_3 through sublimation, the annealing was started at 673 K. Thallium molybdate, Tl_2MoO_4 , was obtained by the following reaction: $\text{Tl}_2\text{CO}_3 + \text{MoO}_3 = \text{Tl}_2\text{MoO}_4 + \text{CO}_2$ at 673–823 K for 100 h. When working with thallium compounds, we followed the recommended precautions. This is, of course, a white coat, hand protection and simple gauze mask respiratory. Hafnium molybdate, $\text{Hf}(\text{MoO}_4)_2$, was synthesized by stepwise annealing of stoichiometric mixtures of HfO_2 and MoO_3 at 673–1023 K for 100 h. The starting compounds were well mixed and ground in agate mortar with a pestle. To accelerate the interaction, the reaction mixtures were gradually annealed at the temperatures specified in the interval and ground after every 24 hours of annealing.

Phase relationships in the subsolidus region of the $\text{Tl}_2\text{MoO}_4\text{--In}_2(\text{MoO}_4)_3\text{--Hf}(\text{MoO}_4)_2$ system was studied by the method of “intersecting joins” [49,50]. The phase formation in the $\text{Tl}_2\text{MoO}_4\text{--In}_2(\text{MoO}_4)_3\text{--Hf}(\text{MoO}_4)_2$ system was investigated by the cross-section method in the subsolidus region. We took from the literature information about what compounds are formed in binary systems, which are sides of the studied triangle [51–54]. So, on the side of $\text{Tl}_2\text{MoO}_4\text{--In}_2(\text{MoO}_4)_3$ [51,52], the authors found two compounds of the compositions $\text{TlIn}(\text{MoO}_4)_2$ (1:1) and $\text{Tl}_5\text{In}(\text{MoO}_4)_4$ (5:1). Two composition $\text{Tl}_8\text{Hf}(\text{MoO}_4)_6$ (4:1) and $\text{Tl}_2\text{Hf}(\text{MoO}_4)_3$ (1:1) were found in the $\text{Tl}_2\text{MoO}_4\text{--Hf}(\text{MoO}_4)_2$ system [53]. But inside the $\text{In}_2(\text{MoO}_4)_3\text{--Hf}(\text{MoO}_4)_2$ system, new compounds could not be detected [54]. In order to determine which segments are quasi binary and to reveal the formation of new triple molybdates, we selected about twenty samples. The composition of the samples was determined using the concentration triangle. As a result, we got the following kind of triple $\text{Tl}_2\text{MoO}_4\text{--In}_2(\text{MoO}_4)_3\text{--Hf}(\text{MoO}_4)_2$ system (Fig. 1.). Seven segment $\text{Tl}_5\text{In}(\text{MoO}_4)_4\text{--Tl}_8\text{Hf}(\text{MoO}_4)_6$, $\text{TlIn}(\text{MoO}_4)_2\text{--Tl}_8\text{Hf}(\text{MoO}_4)_6$, $\text{TlIn}(\text{MoO}_4)_2\text{--Tl}_2\text{Hf}(\text{MoO}_4)_3$, $\text{TlIn}(\text{MoO}_4)_2\text{--Hf}(\text{MoO}_4)_2$, $\text{TlIn}(\text{MoO}_4)_2\text{--Tl}_5\text{InHf}(\text{MoO}_4)_6$, $\text{Tl}_5\text{InHf}(\text{MoO}_4)_6\text{--Tl}_8\text{Hf}(\text{MoO}_4)_6$ and $\text{Tl}_5\text{InHf}(\text{MoO}_4)_6\text{--Tl}_2\text{Hf}(\text{MoO}_4)_3$ divide the $\text{Tl}_2\text{MoO}_4\text{--In}_2(\text{MoO}_4)_3\text{--Hf}(\text{MoO}_4)_2$ system into seven subsystems.

$\text{Tl}_5\text{InHf}(\text{MoO}_4)_6$ was synthesized from simple molybdates of thallium, indium, and hafnium at a molar ratio of the corresponding starting components of 5 : 1 : 2. Annealing was carried out in the temperature range of 723–853 K for 80 hours. $\text{Tl}_5\text{InHf}(\text{MoO}_4)_6$ is a white powder. The synthesis of triple molybdate was carried out according to the following reaction:



Molybdate is insoluble in water and organic solvents but dissolves when heated in HCl, H_2SO_4 , and HNO_3 .

--- Figure 1 ---

2.2 Characterization methods

PXRD patterns were recorded on a Bruker D8 ADVANCE X-ray diffractometer (Bruker, Berlin, Germany) with Cu-K α radiation ($\lambda = 1.5418 \text{ \AA}$) at room temperature. The scanning range is between 5 and 100° with a scanning width of 0.02 and a rate of 0.1 s^{-1} .

The variable counting time (VCT) scheme was used to collect the diffraction data of $\text{Tl}_5\text{InHf}(\text{MoO}_4)_6$ for Rietveld analysis. The measurement time was systematically increased towards higher 2θ angles, leading to drastically improved data quality [55,56]. To collect the X-ray data using VCT scheme, five ranges were generated on the diffraction pattern: 5° – 32.0° (exposure per point: 0.5 s; step: 0.0069°), 32.0° – 59.0° (exposure per point: 1 s; step: 0.0069°), 59.0° – 86.0° (exposure per point: 2 s; step: 0.0069°), 86.0° – 113.0° (exposure per point: 4 s; step: 0.0069°) and 113.0° – 140° (exposure per point: 8 s; step: 0.0069°). Total experimental time was equal to ~ 19 h. The esd's $\sigma(I_i)$ of all points on patterns were calculated using intensities I_i ; $\sigma(I_i)=I_i^{1/2}$. The intensities and obtained esd's were further normalized, taking into account actual value of exposition time, and saved in xye-type file. So transformed powder pattern has usual view in whole 2θ range 5 – 140° , but all high-angle points have small esd's.

Differential scanning calorimetry (DSC) was carried out on a NETZSCH STA 449 F1 TG/DSC/DTA (Jupiter) thermal analyzer. The sample charge was 18 mg, and the rate of temperature rise was 10 K/min in the Ar atmosphere. Sample was placed into platinum crucible with lid. The relative error of weight change determination was $\Delta = 1\%$, and that of heat effects was $\Delta = 2$ – 5% . The differential thermal analysis (DTA) curves were calculated using a specially developed program from Netzsch.

The electrical conductivity was measured using a two-contact impedance spectroscopy method with heating and cooling in the frequency range of 1 – 10^6 Hz (impedance meter “Z-1500J”). Ceramic disks for dielectric investigations were prepared by pressing the powders at 100 bar, and sintering at 773 K for 2 h. The disks were 10 mm in diameter and 1.5–2 mm thick. For making electrodes, large surfaces of the discs were covered with colloid platinum, followed by annealing at about 773 K for 1 h.

$$\text{The ionic conductivity } \sigma \text{ was calculated using the formula } \sigma = 4T/\pi D^2 R \quad (1)$$

where T is the thickness of the ceramic in cm, D is diameter in cm, and R is ohmic resistance in Ω .

The geometric-to-X-ray density ratio was used as the criterion for evaluation of the density of the resulting ceramics. The geometric density was calculated by dividing the weight of the sintered sample by its volume estimated from geometric dimensions. The size of the preliminarily polished sample were measured with an accuracy of ± 0.01 mm. The theoretical density was calculated by the equation,

$$\rho_{\text{x-ray}} = 1.66MZ/V, \quad (2)$$

where M is the molecular weight of the formula unit of a substance, Z is the number of formula units, and V is the unit cell volume.

3. Results and discussion

3.1. Phase Formation Study and Subsidiary Phase Relations

The phase dependences in the triple salt system Tl_2MoO_4 – $\text{In}_2(\text{MoO}_4)_3$ – $\text{Hf}(\text{MoO}_4)_2$ was studied in the air by the crossing section's method [46,47]. We took from the literature information about what compounds are formed in binary systems, which are sides of the studied triangle [50–53]. So, on the side of Tl_2MoO_4 – $\text{In}_2(\text{MoO}_4)_3$ [50,51], the authors found two compounds of the compositions $\text{TlIn}(\text{MoO}_4)_2$ (1:1) and $\text{Tl}_5\text{In}(\text{MoO}_4)_4$ (5:1). Two composition $\text{Tl}_8\text{Hf}(\text{MoO}_4)_6$ (4:1) and $\text{Tl}_2\text{Hf}(\text{MoO}_4)_3$ (1:1) were found in the Tl_2MoO_4 – $\text{Hf}(\text{MoO}_4)_2$ system [52]. But inside the $\text{In}_2(\text{MoO}_4)_3$ – $\text{Hf}(\text{MoO}_4)_2$ system, new compounds could not be detected [53]. In order to determine which sections are quasi binary and to reveal the formation of new triple molybdates, we selected about twenty samples. The composition of the samples was determined using the concentration triangle. As a result, we got the following kind of triple Tl_2MoO_4 – $\text{In}_2(\text{MoO}_4)_3$ – $\text{Hf}(\text{MoO}_4)_2$ system (Fig. 1.). The seven joins $\text{Tl}_5\text{In}(\text{MoO}_4)_4$ – $\text{Tl}_8\text{Hf}(\text{MoO}_4)_6$, $\text{TlIn}(\text{MoO}_4)_2$ – $\text{Tl}_8\text{Hf}(\text{MoO}_4)_6$, $\text{TlIn}(\text{MoO}_4)_2$ – $\text{Tl}_2\text{Hf}(\text{MoO}_4)_3$, $\text{TlIn}(\text{MoO}_4)_2$ – $\text{Hf}(\text{MoO}_4)_2$, $\text{TlIn}(\text{MoO}_4)_2$ – $\text{Tl}_5\text{InHf}(\text{MoO}_4)_6$, $\text{Tl}_5\text{InHf}(\text{MoO}_4)_6$ – $\text{Tl}_8\text{Hf}(\text{MoO}_4)_6$ and $\text{Tl}_5\text{InHf}(\text{MoO}_4)_6$ – $\text{Tl}_2\text{Hf}(\text{MoO}_4)_3$ divide the Tl_2MoO_4 – $\text{In}_2(\text{MoO}_4)_3$ – $\text{Hf}(\text{MoO}_4)_2$ system into seven subsystems.

$\text{Tl}_5\text{InHf}(\text{MoO}_4)_6$ was synthesized from simple molybdates of thallium, indium, and hafnium at a molar ratio of the corresponding starting components of 5 : 1 : 2. Annealing was carried out in the temperature range of 723–853 K for 80 hours. $\text{Tl}_5\text{InHf}(\text{MoO}_4)_6$ is a white powder. The synthesis of triple molybdate was carried out according to the following reaction:



Molybdate is insoluble in water and organic solvents but dissolves when heated in HCl, H_2SO_4 , and HNO_3 .

--- Figure 1 ---

3.1. Crystal structure

It was found that the $\text{Tl}_5\text{InHf}(\text{MoO}_4)_6$ is isostructural to the $\text{K}_5\text{InHf}(\text{MoO}_4)_6$ compound, the structure of which was established in [46]. Therefore, the atomic coordinates of the latter were taken as a starting model for the

Rietveld refinement using the TOPAS 4.2 program [57]. The ratio of Hf/In in two sites were refined taking into account that sum of occupancies are equal to 1 in each site. In order to reduce number of refined parameters, only one thermal parameter was refined for all O atoms. Refinement was stable and gave low *R*-factors (Table 1, Figure 2).

--- Figure 2 ---

--- Table 1 ---

Coordinates of atoms and main bond lengths are in Table 2 and Table 3 respectively. The comparison of the $\text{Tl}_5\text{InHf}(\text{MoO}_4)_6$ unit cell parameters obtained by us (Table 1) with the data from [46] ($a = 10.564(1) \text{ \AA}$, $c = 37.632(4) \text{ \AA}$, $V = 3637.0(6) \text{ \AA}^3$) shows their good agreement. The crystallographic data are deposited in Cambridge Crystallographic Data Centre (CSD # 1995678). The data can be downloaded from the site (www.ccdc.cam.ac.uk/data_request/cif).

--- Table 2 ---

--- Table 3 ---

The crystal structure of $\text{Tl}_5\text{InHf}(\text{MoO}_4)_6$ is shown in Fig. 3. The structure is a framework consisting and contains alternating mixed (Hf,In) O_6 octahedra connected by MoO_4 tetrahedra. The structure is a three-dimensional framework consisting of alternating (Hf,Fe) O_6 -octahedra connected by MoO_4 -tetrahedra. Each octahedron has common vertices with tetrahedra. The atoms arranged in this way form channels extended along with the *a* and *b* axes, in which thallium atoms are located.

--- Figure 3 ---

3.2. Thermal and electrical properties

The DSC heating curve for a polycrystalline $\text{Tl}_5\text{InHf}(\text{MoO}_4)_6$ sample features two endotherms induced by first-order phase transformation ($T = 837 \text{ K}$, $\Delta H = -2.27 \text{ J / g}$), namely, polymorphic transition (Fig. 4) and melting of molybdate ($T = 941 \text{ K}$, $\Delta H = -47.89 \text{ J / g}$). Similar transitions were detected in $\text{K}_5\text{InHf}(\text{MoO}_4)_6$ isostructural compound [44].

Figure 4 shows the results of combined TG/DSC analysis of $\text{Tl}_5\text{InHf}(\text{MoO}_4)_6$ from 380 K temperature to 960 K. DSC heating curve of $\text{Tl}_5\text{InHf}(\text{MoO}_4)_6$ clearly show the endothermic effects corresponding to the first order phase transition at ($T = 837 \text{ K}$, $\Delta H = -2.27 \text{ J / g}$) and incongruently melting of the molybdate at ($T = 941 \text{ K}$, $\Delta H = -47.89 \text{ J / g}$). Similar transitions were detected in $\text{K}_5\text{InHf}(\text{MoO}_4)_6$ isostructural compound [47]. When cooling on the DSC curve, we see exoeffects, related to the crystallization of the compounds into which the molybdate $\text{Tl}_5\text{InHf}(\text{MoO}_4)_6$ is decomposed. During the heating (green curve above) and cooling (green curve below), the TG is very clear and there is no loss in weight. This indicates the complete absence of volatile impurities.

--- Figure 4 ---

The main and reliable method for study electrical processes in ion-conducting compounds is impedance spectroscopy. Figure 5 shows the impedance diagrams for $\text{Tl}_5\text{InHf}(\text{MoO}_4)_6$ at different temperatures.

--- Figure 5 ---

Figure 5a,b shows that at low temperatures, the impedance diagram consists of two parts. One of them has the shape of an arch at high frequencies, and the second has the shape of a line at low frequencies. This indicates the presence of two relaxation phenomena. The arc, which is located at higher frequencies, corresponds to the movement of ions through the grain (volume), which represents the intrinsic conduction and gives rise to intragranular resistance. The line describes the processes of movement of ions across grain boundaries. At higher temperatures (about 712 K), three semicircles making up the impedance can be seen. A small semicircle is associated with charge transfer at the molybdate-electrode interface. This form of hodograph is characteristic of materials with ionic transport. At even higher temperatures (Fig. 5e), this semicircle degenerates, indicating that the diffusion layer has a finite thickness.

Figure 6 shows the temperature dependences of the resistivity on the inverse temperature obtained by heating and cooling ceramics at different frequencies (from 1 Hz to 1 MHz). In the region of 800 K, an anomaly of conductivity is observed due to a phase transition. The temperature hysteresis, which is characteristic of, which is

accompanied by an increase in conductivity, is clearly visible. The transition temperature corresponds to the differential thermal analysis (Fig. 4).

--- Figure 6 ---

Figure 5 shows the temperature dependences of the conductivity on the versus reciprocal temperature obtained by heating and cooling ceramics at different frequencies (from 1 Hz to 1 MHz). The density of ceramics was 79 %. In the region of 800 K, an anomaly of conductivity is observed due to a phase transition. The temperature hysteresis, which is characteristic of, which is accompanied by an increase in conductivity, is clearly visible. The transition temperature corresponds to the differential thermal analysis (Fig. 4).

--- Figure 5 ---

Figure 6 shows the complex impedance (imaginary $-Z''$ versus real Z') plots at different temperatures ranging from 473 to 853 K under air for the $Tl_5InHf(MoO_4)_6$ sample. The diagrams at temperatures up to 573 K shows the patterns of a deformed semicircular arc and a low-frequency tail. The appearance of the tail at lower frequency may be owing to the polarized phenomena associated with the thallium-ion conduction across the electrolyte/electrode boundary. Graphs obtained in the form of deformed semicircular arcs show the presence of two overlapping semicircles with reaching zero on Z' -axis and Z'' -axis in the high-frequency region (Fig. 6). For a high-frequency semicircle, the capacitance values are of the order of 10^{-10} F, which can be considered as the average value of capacitance for bulk and grain-boundary conductivity (10^{-12} and 10^{-8} F). That is, the semicircle is associated both with both contributions of the bulk and grain boundary. The resistance of the grain boundaries decreases with increasing temperature and, accordingly, the conductivity increases. This behavior is characteristic of solid electrolytes.

--- Figure 6 ---

As can be seen from Fig. 7, the dependence of the electrical conductivity of $Tl_5InHf(MoO_4)_6$ ceramics with an increase in frequency does not substantially change up to a certain value, starting from which it grows exponentially, which, apparently, corresponds to the intergrain contribution to the total conductivity. The total conductivity of the samples increases with increasing temperature, and the boundary frequency shifts to the high-frequency region. The increase in conductivity in the entire studied temperature range at low frequencies is due to an increase in the concentration of the main charge carriers.

--- Figure 7 ---

In accordance with the type of hodographs of impedance select an equivalent circuit using the method of impedance spectroscopy. The shift of the semicircle centers on the hodograph below the abscissa indicates that the system cannot be described by a combination of pure resistances and capacities, but it is necessary to replace all capacities with modified frequency-dependent elements (constant phase element - CPE). In Fig. 8 shows an equivalent circuit that describes well the processes taking place in the system. The impedance of ceramics is contributed by the bulk of ceramic grains, grain boundaries, and electrode-electrolyte interface. The impedance of the electrochemical cell $Pt|Tl_5InHf(MoO_4)_6|Pt$ is the sum of the grain bulk resistance R_b with constant phase element CPE_b connected in parallel, the grain boundary resistance R_{gb} with constant phase element CPE_{gb} connected in parallel, and the electrode impedance Z_{el} .

--- Figure 8 ---

From the analysis of complex impedance was obtained temperature dependence of the DC conductivity of $Tl_5InHf(MoO_4)_6$ molybdate. In Fig. 9, for clarity, the dependence is presented in Arrhenius coordinates.

--- Figure 9 ---

The graph observes two linear sections with different slopes. Dependency is well described Arrhenius – Frenkel law, i.e., processes are thermal activation.

The activation energy was calculated using the following formula

$$\sigma_{dc} = \sigma_0 \exp(-E_a/k_b T) \quad (3)$$

In this relation, E_a is the activation energy, k_b is the Boltzmann constant and σ_0 is a constant.

Above the phase transition, the ionic conductivity of the obtained compound reaches $9.8 \times 10^{-4} \text{ S cm}^{-1}$ (853 K) and the activation energy is 0.85 eV. This value are compatible with the cationic conductivity mechanism. Based on the structure of the compound presented in this article, the ionic conductivity observed in $\text{Tl}_5\text{InHf}(\text{MoO}_4)_6$ is most probably due to monovalent Tl^+ cation anisotropic mobility. The alkali metals substitution in the group of $M_5\text{RA}(\text{MoO}_4)_6$ (where $M = \text{K, Rb, Cs}$, $R = \text{lanthanide trivalent ion, Al}^{3+}, \text{Cr}^{3+}, \text{Fe}^{3+}, \text{In}^{3+}, \text{Sc}^{3+}, \text{Y}^{3+}, \text{Bi}^{3+}$, $A = \text{Zr}^{4+}$ or Hf^{4+}) compounds for thallium did not lead to an increase in conductivity. Conductivity of $\text{Tl}_5\text{InHf}(\text{MoO}_4)_6$ commensurate with the conductivity of $\text{Cs}_5\text{AlZr}(\text{MoO}_4)_6$ ($\sigma = 0.8 \times 10^{-4} \text{ S cm}^{-1}$ at 673 K), $\text{Cs}_5\text{BiZr}(\text{MoO}_4)_6$ ($\sigma = 0.7 \times 10^{-4} \text{ S cm}^{-1}$ at 673 K), $\text{Cs}_5\text{FeZr}(\text{MoO}_4)_6$ ($\sigma = 1.2 \times 10^{-4} \text{ S cm}^{-1}$ at 673 K), $\text{Cs}_5\text{AlZr}(\text{MoO}_4)_6$ ($\sigma = 0.8 \times 10^{-4} \text{ S cm}^{-1}$ at 673 K) [58], $\text{Rb}_5\text{CeHf}(\text{MoO}_4)_6$ ($\sigma = 1.7 \times 10^{-3} \text{ S cm}^{-1}$ at 723 K), $\text{Rb}_5\text{YbHf}(\text{MoO}_4)_6$ ($\sigma = 1.7 \times 10^{-3} \text{ S cm}^{-1}$ at 723 K) [48], $\text{K}_5\text{ScHf}(\text{MoO}_4)_6$ ($\sigma = 1.1 \times 10^{-3} \text{ S cm}^{-1}$ at 900 K) [59], $\text{K}_5\text{RZr}(\text{MoO}_4)_6$ ($R = \text{Al, Cr, Fe, In, Sc}$) ($\sigma \sim 10^{-3} \text{ S cm}^{-1}$ at 723 □ 873 K) [15] compounds. It should be noted that the conductivity is close to those of the NASICON-type conductors and comparable or even better than that of ionic conductors, such as molybdates with lyonsite-type structure. For comparison, the conductivity for $\text{LiNbFe}(\text{PO}_4)_3$ ($\sigma = 6.6 \times 10^{-6} \text{ S cm}^{-1}$), $\text{LiNbFe}(\text{PO}_4)_3$ ($\sigma = 6.6 \times 10^{-6} \text{ S cm}^{-1}$), $\text{LiZr}_2(\text{PO}_4)_3$ ($\sigma = 5 \times 10^{-4} \text{ S cm}^{-1}$) at 573 K [60– 63]. In the system $\text{Li}_{2+x}\text{Mg}_{2(1-x)}\text{Fe}_x(\text{MoO}_4)_3$ with lyonsite-type structure, conductivity ranges at 573 K from 1.1×10^{-7} for $\text{Li}_2\text{Mg}_2(\text{MoO}_4)_3$ to $6.6 \times 10^{-7} \text{ S cm}^{-1}$ for $\text{Li}_3\text{Fe}(\text{MoO}_4)_3$ [10].

Figure 7 shows the variation of the real part of impedance (Z') with frequency at different temperatures for $\text{Tl}_5\text{InHf}(\text{MoO}_4)_6$.

--- Figure 7 ---

In the low frequency region, Z' has maximum values, which decreases with a gradual increase in frequency. By increasing the temperature, the magnitude of Z' decreases which may be due to increase in conductivity of the molybdate. Fig. 8 illustrates the imaginary part of the impedance Z'' with respect to the frequency at different temperatures.

--- Figure 8 ---

On the curves, we observe two peaks. One of them is small. It is located in the low-frequency region. As the temperature increases, the peak shifts to the mid-frequency region. Perhaps it is associated with the relaxation of grain boundaries. The second peak is in the high-frequency region. The maximum value of this peak decreases with increasing temperature and it has certain values at different frequencies. In addition, the peak shifts when heated toward higher frequencies and becomes more blurry. This is due to the presence of space charges in ceramics.

4. Conclusions

We have studied phase relations of the ternary system $\text{Tl}_2\text{MoO}_4\text{--In}_2(\text{MoO}_4)_3\text{--Hf}(\text{MoO}_4)_2$ and us to reveal a novel $\text{Tl}_5\text{InHf}(\text{MoO}_4)_6$ molybdate. The phase relations of the ternary system $\text{Tl}_2\text{MoO}_4\text{--In}_2(\text{MoO}_4)_3\text{--Hf}(\text{MoO}_4)_2$ were studied and a new molybdate $\text{Tl}_5\text{InHf}(\text{MoO}_4)_6$ was discovered. The study of a new thallium indium hafnium molybdate using PXRD showed that the compound has trigonal space group $R\bar{3}c$: $a = 10.63893$ (5) Å, $c = 38.1447$ (3) Å; $V = 3739.04$ (4) Å³, $Z = 6$. It was established in the work that the structure is a framework consisting of alternating mixed (Hf,In)O₆ octahedra connected by MoO₄ tetrahedra. Each octahedron has common vertices with tetrahedrons. The atoms arranged in this way form channels extended along with the a and b axes, in which thallium atoms are located. Impedance spectroscopy was used to investigate the electrical properties of $\text{Tl}_5\text{InHf}(\text{MoO}_4)_6$ ceramics. Analysis of the impedance diagram showed the contribution to the bulk and grain boundaries. It should be noted that the conductivity of the compound $\text{K}_5\text{ScHf}(\text{MoO}_4)_6$ [59] almost did not change its value when potassium was replaced by thallium. Both above and below the phase transition, the dependences are well described by the Arrhenius law.

Acknowledgments

This study was carried out within the state assignment of FASO of Russia (Theme No 0339-2016-0007) as well was supported by RFBR Grants 18-08-00799 and 18-03-00557.

References

[1] Lv DD, Zhang DF, Pu XP, Gao MC, Ma HY, Li HY, Zhang TT (2015). Combustion synthesis of $\text{Li}_8\text{Bi}_2(\text{MoO}_4)_7$ and photocatalytic properties. *Mater Lett* 144: 150–152. doi:10.1016/j.matlet.2015.01.062

- [2] Tsyrenova GD, Solodovnikov SF, Khaikina EG, Khobrakova ET, Bazarova ZG, Solodovnikova ZA (2004). Phase formation in the systems $\text{Ag}_2\text{MoO}_4\text{-MO-MoO}_3(M)\text{Ca, Sr, Ba, Pb, Cd, Ni, Co, Mn}$ and crystal structures of $\text{Ag}_2\text{M}_2(\text{MoO}_4)_3 (M = \text{Co, Mn})$. *J Solid State Chem* 177: 2158–2167. <https://doi.org/10.1016/j.jssc.2004.01.002>
- [3] Nasri R, Larbi T, Amlouk M, Zid MF (2018). Investigation of the physical properties of $\text{K}_2\text{Co}_2(\text{MoO}_4)_3$ for photocatalytic application. *J Mater Sci Mater Electron* 29: 18372–18379. <https://doi.org/10.1007/s10854-018-9951-x>
- [4] Lu Y, Li Y, Huang Y, Chen C, Cai P, Seo HJ (2015). A visible-light-driven photocatalyst of NASICON $\text{Li}_2\text{Ni}_2(\text{MoO}_4)_3$ nanoparticles. *J Am Ceram Soc* 98: 2165–2169. <https://doi.org/10.1111/jace.13612>
- [5] Loiko P, Vilejshikova EV, Volokitina AA, Trifonov VA, Serres JM, Mateos X, Kuleshov NV, Yumashev KV, Baranov AV, Pavlyuk AA (2017). Growth, structure, Raman spectra and luminescence of orthorhombic $\text{Li}_2\text{Mg}_2(\text{MoO}_4)_3$ crystals doped with Eu^{3+} and Ce^{3+} ions. *J Lumin* 188: 154–161. <https://doi.org/10.1016/j.jlumin.2017.04.021>
- [6] Lu D, Gong X, Chen Y, Huang J, Lin Y, Luo Z, Huang Y (2018). Synthesis and photoluminescence characteristics of the $\text{LiGd}_3(\text{MoO}_4)_5: \text{Eu}^{3+}$ red phosphor with high color purity and brightness. *Opt Mater Express* 8: 259–269. <https://doi.org/10.1364/OME.8.000259>
- [7] Wang GQ, Li LY, Feng YN, Yu H, Zheng XH (2018). Tb^{3+} and Yb^{3+} -doped novel $\text{KBaLu}(\text{MoO}_4)_3$ crystals with disordered chained structure showing down- and upconversion luminescence. *CrystEngComm* 20: 3657–3665. <https://doi.org/10.1039/C8CE00461G>
- [8] Ines E, Zid MF, Driss A (2013). Synthesis, crystal structure and electrical properties of the molybdenum oxide $\text{Na}_{1.92}\text{Mg}_{2.04}\text{Mo}_3\text{O}_{12}$. *J of Crystallograph* 2013: 1–6. <https://doi.org/10.1155/2013/146567>
- [9] Nasri R, Marzouki R, Georges S, Obbade S, Zid MF (2018). Synthesis, sintering, electrical properties and sodium migration pathways of new lyonsite $\text{Na}_2\text{Co}_2(\text{MoO}_4)_3$. *Turk J Chem* 42: 1–31. <https://doi.org/10.3906/kim-1801-89>
- [10] Sebastian L, Piffard Y, Shukla AK, Taulelle F, Gopalakrishnan J (2003). Synthesis, structure and lithium-ion conductivity of $\text{Li}_{2-2x}\text{Mg}_{2+x}(\text{MoO}_4)_3$ and $\text{Li}_3M(\text{MoO}_4)_3 (M = \text{Cr, Fe})$. *J Mater Chem* 13: 1797–1802. <https://doi.org/10.1039/B301189E>
- [11] Prabakaran SRS, Fauzi A, Michael MS, Begam KM (2004). New NASICON-type $\text{Li}_2\text{Ni}_2(\text{MoO}_4)_3$ as a positive electrode material for rechargeable lithium batteries. *Solid State Ionics* 17: 157–165. <https://doi.org/10.1016/j.ssi.2004.05.001>
- [12] Begam K, Selladurai S (2004). Synthesis and redox behavior of a new polyanion compound, $\text{Li}_2\text{Co}_2(\text{MoO}_4)_3$, as 4 V class positive electrode material for lithium batteries. *Ionics* 10: 77–83. <https://doi.org/10.1007/BF02410310>
- [13] Zapart MB, Zapart W, Maczka M (2016). Complex ferroelastic domain patterns of $\text{K}_{1-x}\text{Rb}_x\text{Sc}(\text{MoO}_4)_2$ crystals. *Ferroelectrics* 1: 34–41. <https://doi.org/10.1080/00150193.2016.1160729>
- [14] Zapart W, Zapart MB (2013). Phase transitions in ferroelastic $\text{RbIn}(\text{MoO}_4)_2$ at 163 and 143 K. *Ferroelectrics* 1: 116–120. <https://doi.org/10.1080/00150193.2013.839289>
- [15] Bazarova JG, Logvinova AV, Bazarov BG, Tushinova YL, Dorzhieva SG, Temujin J (2018). Synthesis of new triple molybdates $\text{K}_5\text{RZr}(\text{MoO}_4)_6 (R = \text{Al, Cr, Fe, In, Sc})$ in the $\text{K}_2\text{MoO}_4\text{-R}_2(\text{MoO}_4)_3\text{-Zr}(\text{MoO}_4)_2$ systems, their structure and electrical properties. *J Alloy Comp* 741: 834–839. <https://doi.org/10.1016/j.jallcom.2018.01.208>
- [16] Yudin VN, Zolotova ES, Solodovnikov SF, Solodovnikova ZA, Korolkov IY, Stefanovich SYu, Kuchumo BM (2019). Synthesis, structure, and conductivity of alluaudite-related phases in the $\text{Na}_2\text{MoO}_4\text{-Cs}_2\text{MoO}_4\text{-CoMoO}_4$ system. *Eur J Inorg Chem* 277–286. <https://doi.org/10.1002/ejic.201801307>
- [17] Savina AA, Solodovnikov SF, Belov DA, Solodovnikova ZA, Stefanovich SYu, Lazoryakd BI, Khaikina EG (2017). New alluaudite-related triple molybdates $\text{Na}_{25}\text{Cs}_8\text{R}_5(\text{MoO}_4)_{24} (R = \text{Sc, In})$: synthesis, crystal structures and properties. *New J Chem* 41: 5450–5457. <https://doi.org/10.1039/C7NJ00202E>
- [18] Kotova IYu, Solodovnikov SF, Solodovnikova ZA, Belov DA, Stefanovich SYu, Savina AA, Khaikina EG (2016). New series of triple molybdates $\text{AgA}_3\text{R}(\text{MoO}_4)_5 (A = \text{Mg, R} = \text{Cr, Fe; A} = \text{Mn, R} = \text{Al, Cr, Fe, Sc, In})$ with framework structures and mobile silver ion sublattices. *J Solid State Chem* 238: 121–128. <https://doi.org/10.1016/j.jssc.2016.03.003>
- [19] Xue J, Li H, Noh HM, Choi BC, Park SH, Jeong JH, Kim JH (2018). Molybdenum substitution induced luminescence enhancement in $\text{Gd}_2\text{W}_{1-x}\text{Mo}_x\text{O}_6: \text{Eu}^{3+}$ phosphors for near ultraviolet based solid-state lighting. *J Lumin* 202: 97–106. doi:10.1016/j.jlumin.2018.05.033
- [20] Solodovnikov SF, Khaikina EG, Solodovnikova ZA, Kadyrova YuM, Khal'baeva KM, Zolotova ES (2007). New families of lithium-containing triple molybdates and the stabilizing role of lithium in their structure formation. *Dokl Chem* 416: 207–212. doi:10.1134/S0012500807090029
- [21] Khaikina EG, Bazarova ZhG, Solodovnikov SF, Klevtsova RF (2011). Troynye molibdaty kak osnova novykh perspektivnykh slozhnooksidnykh materialov. *Eng Ecol* 1: 48–49
- [22] Morozov VA, Lazoryak BI, Smirnov VA, Mikhailin VV, Basovich OM, Khaikina EG (2001). Crystal structures and luminescence properties of ternary molybdates $\text{LiMNd}_2(\text{MoO}_4)_4 (M = \text{K, Rb, Tl})$. *Russ J Inorg Chem* 46: 873–879
- [23] Zhou L, Du P (2019). Sol-gel synthesis of $\text{CaLa}_2(\text{MoO}_4)_4 \cdot 2x\text{Sm}^{3+}$ microparticles: a red-emitting phosphor with splendid thermal stability for near-ultraviolet based white light-emitting diodes. *Appl Phys A Mater Sci Process* 125: 282–285

- [24] Lim CS, Aleksandrovsky AS, Molokeev MS, Oreshonkov AS, Ikonnikov DA, Atuchin VV (2016). Triple molybdate scheelite-type upconversion phosphor $\text{NaCaLa}(\text{MoO}_4)_3\text{:Er}^{3+}/\text{Yb}^{3+}$: structural and spectroscopic properties. *Dalton Trans* 45: 15541. doi:10.1039/c6dt02378a
- [25] Lim CS, Aleksandrovsky AS, Molokeev MS, Oreshonkov AS, Atuchin VV (2017). Microwave synthesis and spectroscopic properties of ternary scheelite-type molybdate phosphors $\text{NaSrLa}(\text{MoO}_4)_3\text{:Er}^{3+}, \text{Yb}^{3+}$. *J Alloy Comp* 713: 156–163
- [26] Hong HJ (1976). Crystal-structures and crystal-chemistry in system $\text{Na}_{1-x}\text{Zr}_2\text{Si}_x\text{P}_{3-x}\text{O}_{12}$. *Mat Res Bull* 11: 173–182. doi:10.1016/0025-5408(76)90073-8
- [27] Velikodny YuA (1975) Double molybdates and tungstates of alkali metals with indium and scandium Dissertation, Moscow
- [28] Lazoryak BI, Efremov VA (1987). Phases of $\text{Na}_{2x}\text{Zn}_2\text{Sc}_{2(1-x)}\text{-II}(\text{MoO}_4)_3$, $\text{Na}_{2x}\text{Cd}_2\text{Sc}_{2(1-x)}\text{-II}(\text{MoO}_4)_3$, $\text{Na}_{2x}\text{Mg}_2\text{Sc}_{2(1-x)}\text{-II}(\text{MoO}_4)_3$ changed composition. *Zh Neorg Khim* 32: 652–656
- [29] Kozhevnikova NM, Mokhosoev MV (1992). Triple molybdates. *Zh Neorg Khim* 37: 2395–2401
- [30] Kotova IYu, Belov DA, Stefanovich SYu (2011). $\text{Ag}_{1-x}\text{Mg}_{1-x}\text{R}_{1+x}(\text{MoO}_4)_3$ Ag^+ -Conducting NASICON-Like Phases, where $R = \text{Al}$ or Sc and $0 \leq x \leq 0.5$. *Russ J Inorg Chem* 56: 1259–1263. doi:10.1134/S0036023611080122
- [31] Ines E, Samuel G, Youssef BS, Abderrahmen G, Zid MF, Boughazala H (2015). Synthesis, crystal structure, sintering and electrical properties of a new alluaudite-like triple molybdate $\text{K}_{0.13}\text{Na}_{3.87}\text{MgMo}_3\text{O}_{12}$. *RSC Advances* 5: 38918–38925. doi:10.1039/c5ra02276b
- [32] Bazarova JG, Tushinova YuL, Bazarov BG, Oyun BE, Angarhayev JD (2018). Phase equilibrium in the systems $\text{Cs}_2\text{MoO}_4\text{-R}_2(\text{MoO}_4)_3\text{-Hf}(\text{MoO}_4)_2$ ($R = \text{Al}, \text{Cr}, \text{Fe}, \text{Bi}, \text{La-Lu}$). *Izvestiya vuzov-prikladnaya khimiya i biotekhnologiya* 8: 19–28. doi:10.21285/2227-2925-2018-8-2-19-28
- [33] Grossman VG, Bazarova JG, Molokeev MS, Bazarov BG (2020). New triple molybdate $\text{K}_5\text{ScHf}(\text{MoO}_4)_6$: Synthesis, properties, structure and phase equilibria in the $M_2\text{MoO}_4\text{-Sc}_2(\text{MoO}_4)_3\text{-Hf}(\text{MoO}_4)_2$ ($M = \text{Li}, \text{K}$) systems. *J Solid State Chem* 283: 121143. <https://doi.org/10.1016/j.jssc.2019.121143>
- [34] Dorzhieva SG, Bazarov BG, Bazarova JG (2019). New molybdates in the $\text{Rb}_2\text{MoO}_4\text{-(M}_2\text{MoO}_4)\text{-M-IZr}(\text{MoO}_4)_2$ ($M = \text{Na}, \text{K}$) systems as promising ion-conducting materials. *Letters on materials* 9: 17–21. doi:10.22226/2410-3535-2019-1-17-21
- [35] Logvinova AV, Bazarov BG, Tushinova YuL, Bazarova JG (2017). Phase Relations in the $\text{K}_2\text{MoO}_4\text{-Ln}_2(\text{MoO}_4)_3\text{-Zr}(\text{MoO}_4)_2$ ($\text{Ln} = \text{La-Lu}, \text{Y}$) Systems. *Inorg Mater* 53: 1286–1292. doi:10.1134/S0020168517120081
- [36] Grossman VG, Bazarov BG, Bazarova TsT, Glinskaya LA, Bazarova JG, Temuujiin J (2017). Phase equilibria in the $\text{Ti}_2\text{MoO}_4\text{-Ho}_2(\text{MoO}_4)_3\text{-Zr}(\text{MoO}_4)_2$ system and the crystal structure of $\text{Ho}_2\text{Zr}_2(\text{MoO}_4)_7$ and $\text{TiHoZr}_{0.5}(\text{MoO}_4)_3$. *J Ceram Proc Res* 18: 875–881
- [37] Gongorova LI, Bazarov BG, Chimitova OD, Anshits AG, Vereschagina TA, Klevtsova RF, Glinskaya LA, Bazarova ZG (2012). Crystal structure of a new ternary molybdate $\text{Rb}_5\text{CeZr}(\text{MoO}_4)_6$. *J Struct Chem* 53: 329–333. doi:10.1134/S0022476612020175
- [38] Chimitova OD, Bazarov BG, Klevtsova RF, Anshits AG, Fedorov KN, Dubentsov AV, Vereshchagina TA, Tushinova YuL, Glinskaya LA, Bazarova ZhG, Gongorova LI (2010). Crystal structure of triple molybdate in the $\text{Rb}_2\text{MoO}_4\text{-Nd}_2(\text{MoO}_4)_3\text{-Zr}(\text{MoO}_4)_2$ system. *J Struct Chem* 51: 173–176. doi:10.1007/s10947-010-0025-z
- [39] Namsaraeva TV, Bazarov BG, Klevtsova RF, Glinskaya LA, Fedorov KN, Bazarova ZhG (2010). Subsolidus Phase Equilibrium in $\text{Cs}_2\text{MoO}_4\text{-Al}_2(\text{MoO}_4)_3\text{-Zr}(\text{MoO}_4)_2$ System and Crystal Structure of New Ternary Molybdate $\text{Cs}(\text{AlZr}_{0.5})(\text{MoO}_4)_3$. *Russ J Inorg Chem* 55: 209–214. doi:10.1134/S0036023610020129
- [40] Bazarov BG, Namsaraeva TV, Klevtsova RF, Anshits AG, Vereshchagina TA, Kurbatov RV, Glinskaya LA, Fedorov KN, Bazarova ZhG (2008). Phase equilibrium in the $\text{Cs}_2\text{MoO}_4\text{-Bi}_2(\text{MoO}_4)_3\text{-Zn}(\text{MoO}_4)_2$ system and the crystal structure of new triple molybdate $\text{Cs}_5\text{BiZr}(\text{MoO}_4)_6$. *Russ J Inorg Chem* 53: 1484–1488. doi:10.1134/S0036023608090222
- [41] Bazarov BG, Chimitova OD, Bazarova TsT, Arkhincheeva SI, Bazarova ZhG (2008). Phase relations in the systems $M_2\text{MoO}_4\text{-Cr}_2(\text{MoO}_4)_3\text{-Zr}(\text{MoO}_4)_2$ ($M = \text{Li}, \text{Na}, \text{or Rb}$). *Russ J Inorg Chem* 53: 959–961. doi:10.1134/S0036023608060247
- [42] Bazarov BG, Chimitova OD, Klevtsova RF, Tushinova YuL, Glinskaya LA, Bazarova ZhG (2008). Crystal structure of a new ternary molybdate in the $\text{Rb}_2\text{MoO}_4\text{-Eu}_2(\text{MoO}_4)_3\text{-Hf}(\text{MoO}_4)_2$ system. *J Struct Chem* 49: 53–57. doi:10.1007/s10947-008-0008-5
- [43] Chimitova OD, Bazarov BG, Klevtsova RF, Fedorov KN, Glinskaya LA, Kuznetsov MV, Bazarova ZhG (2007). Synthesis, crystal structure, and electrical properties of the new ternary molybdate $\text{Rb}_5\text{NdHf}(\text{MoO}_4)_6$. *Russ Chem Bull* 56: 2135–2139. doi:10.1007/s11172-007-0337-0
- [44] Romanova EYu, Bazarov BG, Klevtsova RF, Glinskaya LA, Tushinova YuL, Fedorov KN, Bazarova ZhG (2007). Phase formation in the $\text{K}_2\text{MoO}_4\text{-Lu}_2(\text{MoO}_4)_3\text{-Hf}(\text{MoO}_4)_2$ system and the structural study of triple molybdate $\text{K}_5\text{LuHf}(\text{MoO}_4)_6$. *Russ J Inorg Chem* 52: 749–752. doi:10.1134/S0036023607050154
- [45] Bazarov BG, Klevtsova RF, Chimitova OD, Glinskaya LA, Fedorov KN, Tushinova YuL, Bazarova ZhG (2006). Phase formation in the $\text{Rb}_2\text{MoO}_4\text{-Er}_2(\text{MoO}_4)_3\text{-Hf}(\text{MoO}_4)_2$ system and the crystal structure of new triple molybdate $\text{Rb}_5\text{ErHf}(\text{MoO}_4)_6$. *Russ J Inorg Chem* 51: 800–804. doi:10.1134/S0036023606050196
- [46] Bazarov BG, Klevtsova RF, Bazarova TT, Glinskaya LA, Fedorov KN, Bazarova ZhG (2005). Synthesis and crystal structure of triple molybdate $\text{K}_5\text{InHf}(\text{MoO}_4)_6$. *Russ J Inorg Chem* 50: 1146–1149

- [47] Grossman VG, Bazarov BG, Bazarova JG (2019). $K_5\text{InHf}(\text{MoO}_4)_6$: A solid state conductor. IOP Conference Series: Earth and Environmental Science 320: 012050
- [48] Chimitova OD, Bazarov BG, Fedorov KN, Bazarova ZhG (2008). Electrical properties of triple molybdates $\text{Rb}_5\text{LnHf}(\text{MoO}_4)_6$. Russ. J. Appl. Chem. 81: 2043–2044
- [49] Guertler WZ (1926). Zur Fortentwicklung der Konstitutionsforschungen bei ternären Systemen. Anorg Allg Chem Bd 154: 439–455
- [50] Niepel L, Malinovsky M (1978). Triangulation of phase diagrams. Chem Zvesti 32: 810–820
- [51] Sul'timova LB, Burdakova IB, Khaikina EG, Bazarova ZG (2000). $\text{Ti}_2\text{MoO}_4\text{--R}_2(\text{MoO}_4)_3$ ($R = \text{In, Sc}$) systems. Russ J Inorg Chem 45: 1900–1904
- [52] Pleskov MY, Morozov VA, Lazoryak BI, Zhizhin MG, Burdakova IB, Khal'baeva KM, Tsyrenova GD, Khaikina EG (2005). Structures of double molybdates $\text{TiR}(\text{MoO}_4)_2$ ($R = \text{In, Sc, Fe, Cr, Al}$). Russ J Inorg Chem 50: 604–614
- [53] Bazarov BG, Klevtsova RF, Bazarova TsT, Glinskaya LA, Fedorov KN, Bazarova ZhG, Chimitova OD (2006). Systems $\text{Ti}_2\text{MoO}_4\text{--E}(\text{MoO}_4)_2$, where $E = \text{Zr}$ or Hf , and the crystal structure of $\text{Ti}_8\text{Hf}(\text{MoO}_4)_6$. Russ J Inorg Chem 51: 794–799. doi:10.1134/S0036023606050184
- [54] Tushinova YuL, Bazarova JG, Arkhincheeva SI (2002). Phase equilibria in systems $\text{R}_2(\text{MoO}_4)_3\text{--Zr}(\text{MoO}_4)_2$, Vsesos. scientific reading from int. participation, dedicated. 70th birthday of member USSR Academy of Sciences M.V. Mokhosoeva. Publishing House of the BSC SB RAS. 90–91
- [55] Madsen I, Hill RJ (1992). Variable step-counting times for Rietveld analysis or getting the most out of your experiment time. Adv X-ray Anal 35: 39–47
- [56] Madsen IC, Hill RJ (1994). Collection and Analysis of Powder Diffraction Data with Near-Constant Counting Statistics. J Appl Cryst 27: 385–392
- [57] Bruker AXS TOPAS V4: General profile and structure analysis software for powder diffraction data. – User's Manual. Bruker AXS. Karlsruhe. Germany. 2008.
- [58] Namsaraeva TV (2010) Phase equilibrium, crystalline structures and properties of new double and triple molybdates in systems $\text{Cs}_2\text{MoO}_4\text{--R}_2(\text{MoO}_4)_3\text{--Zr}(\text{MoO}_4)_2$ ($R = \text{Al, Cr, Fe, In, Sc, Bi}$), D. Sc. Dissertation, Irkutsk State University
- [59] Grossman VG, Bazarova JG, Molokeev MS, Bazarov BG (2020). New triple molybdate $\text{K}_5\text{ScHf}(\text{MoO}_4)_6$: Synthesis, properties, structure and phase equilibria in the $\text{M}_2\text{MoO}_4\text{--Sc}_2(\text{MoO}_4)_3\text{--Hf}(\text{MoO}_4)_2$ ($M = \text{Li, K}$) systems. J Solid State Chem 283:121143. doi:10.1016/j.jssc.2019.121143
- [60] Boilot JP, Colin G, Colombar P (1988). Relation structure fast ion conduction in the NASICON solid-solution. J Solid State Chem 73:160–171. doi:10.1016/0022-4596(88)90065-5
- [61] Delmas C, Viola JC, Olazcuaga R, Le Flem G, Hagenmuller P, Cherkaoui F, Brochu R (1981). Ionic-conductivity measurements in the solution $\text{Na}_{1+x}\text{Zr}_{2-x}\text{L}_x(\text{PO}_4)_3$. Mater Res Bull 16:83–90. doi:10.1016/0025-5408(81)90182-3
- [62] Sudreau F, Petit D, Boilot JP (1989). Dimorphism, phase-transitions, and transport-properties in $\text{LiZr}_2(\text{PO}_4)_3$. J Solid State Chem 83:78–90. doi:10.1016/0022-4596(89)90056-X
- [63] Thangadurai V, Shukla AK, Gopalakrishnan J (1999). New lithium-ion conductors based on the NASICON structure. J Mater Chem 9:739–741. doi:10.1039/a807007e

Figures

Figure 1. Phase equilibria of the $\text{Ti}_2\text{MoO}_4\text{--In}_2(\text{MoO}_4)_3\text{--Hf}(\text{MoO}_4)_2$ system in the subsolidus region 803–853K C, where S is $\text{Ti}_5\text{InHf}(\text{MoO}_4)_6$.

Figure 2. Difference Rietveld plot of $\text{Ti}_5\text{InHf}(\text{MoO}_4)_6$.

Figure 3. Projection of the $\text{Ti}_5\text{InHf}(\text{MoO}_4)_6$ structure on (001) plane.

Figure 4. DSC curve of the $\text{Ti}_5\text{InHf}(\text{MoO}_4)_6$.

Figure 5. Impedance spectra of $\text{Ti}_5\text{InHf}(\text{MoO}_4)_6$.

Figure 6. Variation of conductivity (σ , S cm^{-1}) as a function of $1000/T$ for $\text{Ti}_5\text{InHf}(\text{MoO}_4)_6$ sample at 1 Hz to 1 MHz frequencies (heating and cooling).

Figure 7. Variation of real part of impedance (Z') with frequency.

Figure 8. Variation of imaginary part of impedance (Z'') with frequency.

Figure 5. Variation of conductivity σT (K S cm^{-1}) as a function of $1000/T$ (K^{-1}) for $\text{Tl}_5\text{InHf}(\text{MoO}_4)_6$ sample at 1 Hz to 1 MHz frequencies (heating and cooling).

Figure 6. Impedance spectra of $\text{Tl}_5\text{InHf}(\text{MoO}_4)_6$.

Figure 7. Dependence of the conductivity of $\text{Tl}_5\text{InHf}(\text{MoO}_4)_6$ on frequency and temperature.

Figure 8. Equivalent circuit used for calculating the impedance spectra of $\text{Tl}_5\text{InHf}(\text{MoO}_4)_6$.

Figure 9. Plot of $\log(\sigma_{dc}T)$ versus $1000/T$ for $\text{Tl}_5\text{InHf}(\text{MoO}_4)_6$ compound.

Figure 1.

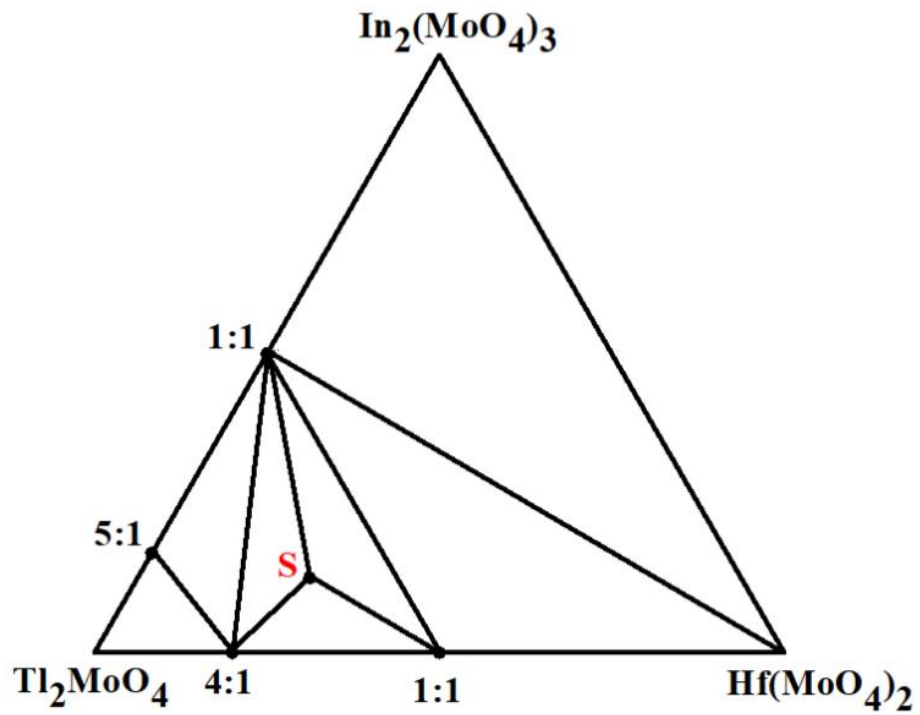


Figure 2.

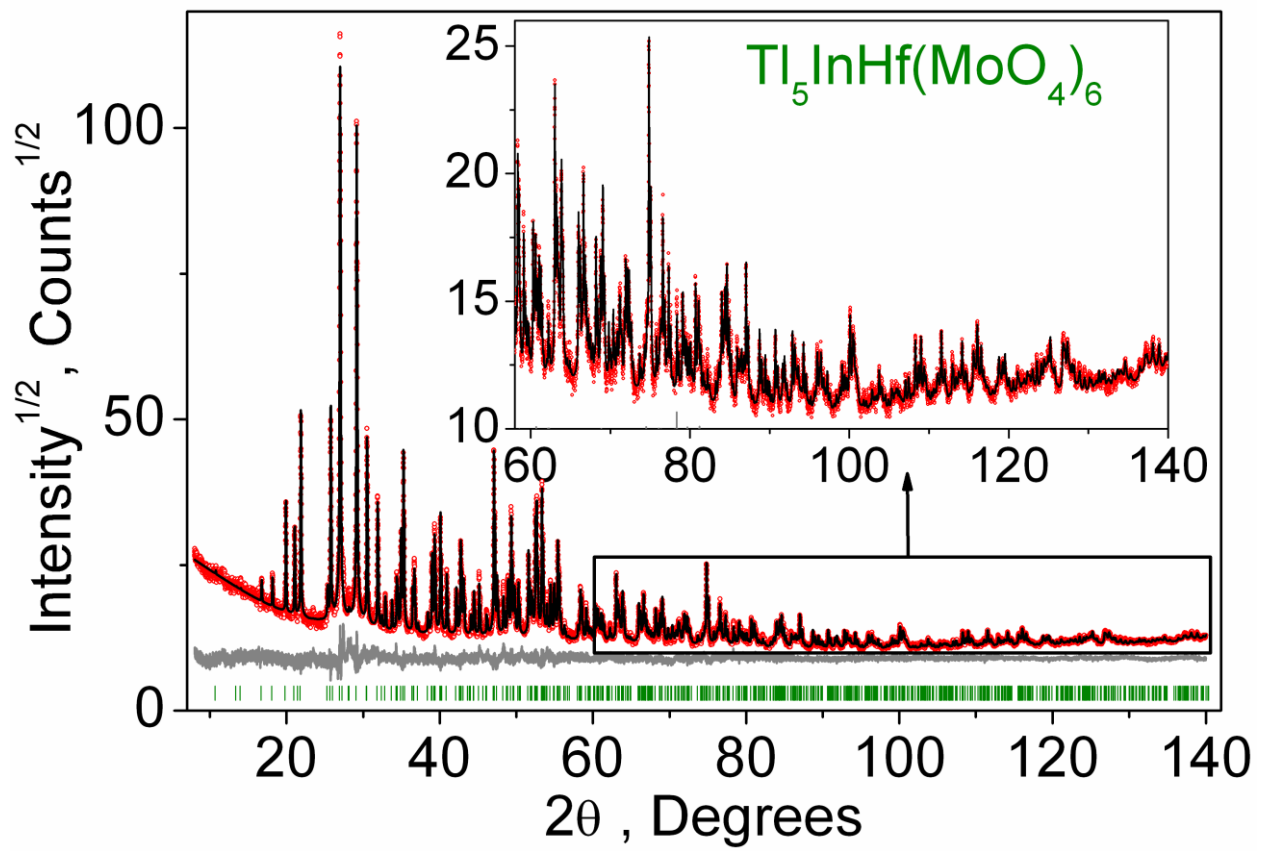


Figure 3.

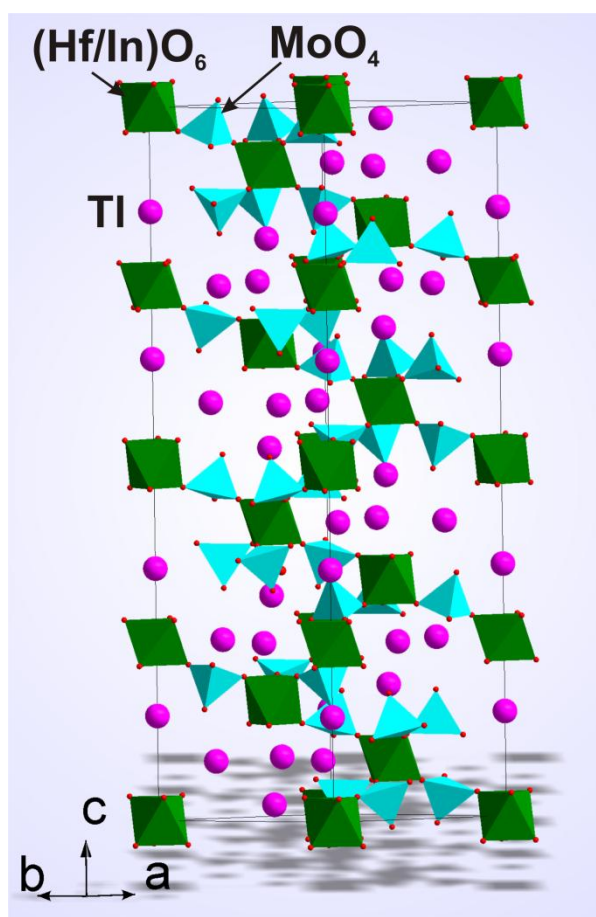


Figure 4.

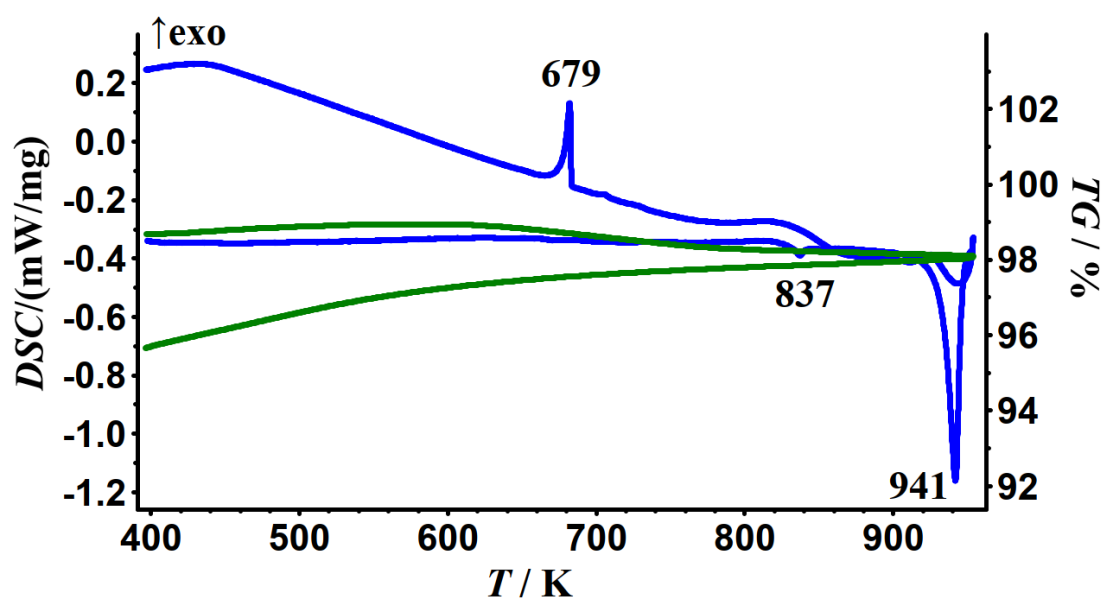
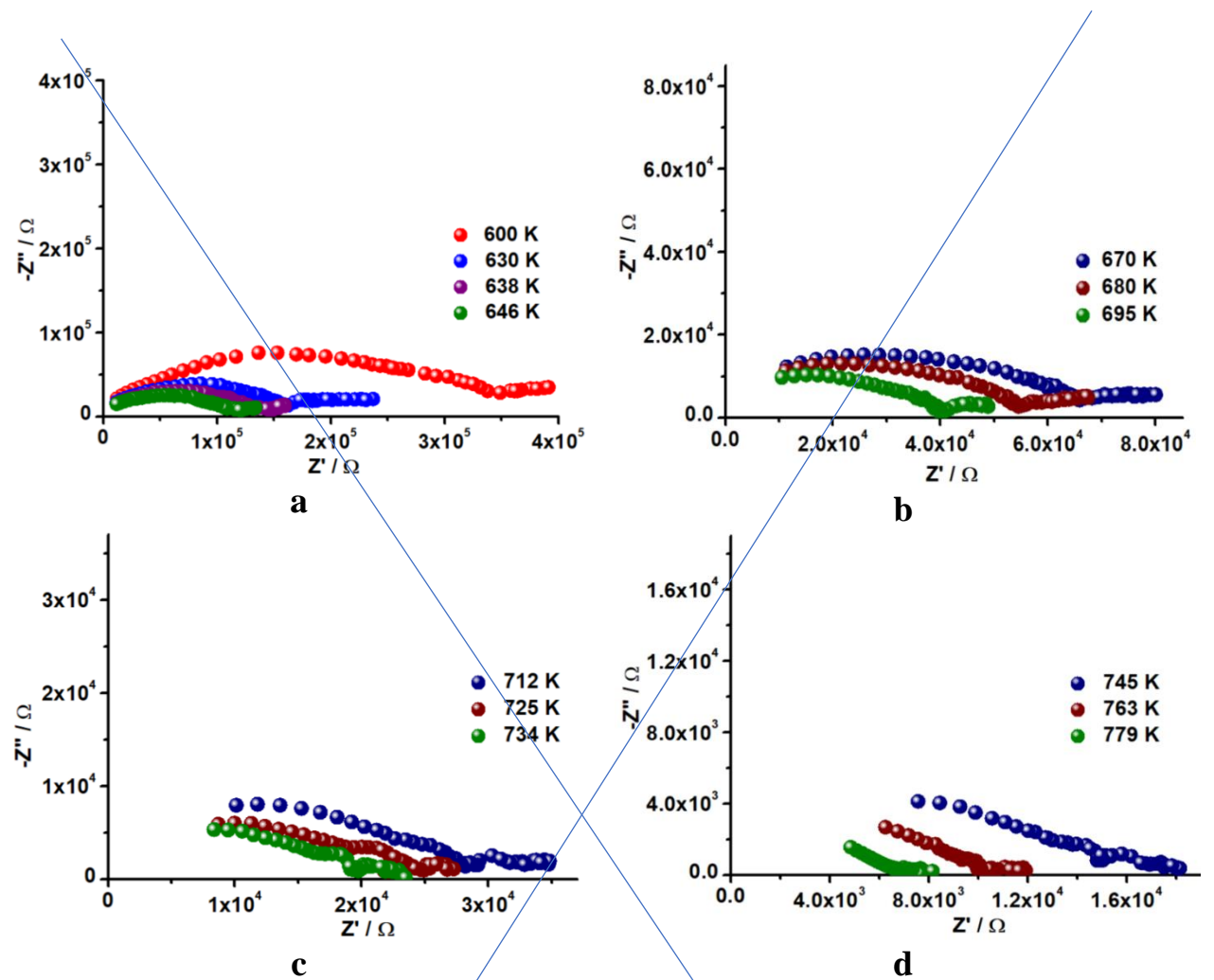


Figure 5.



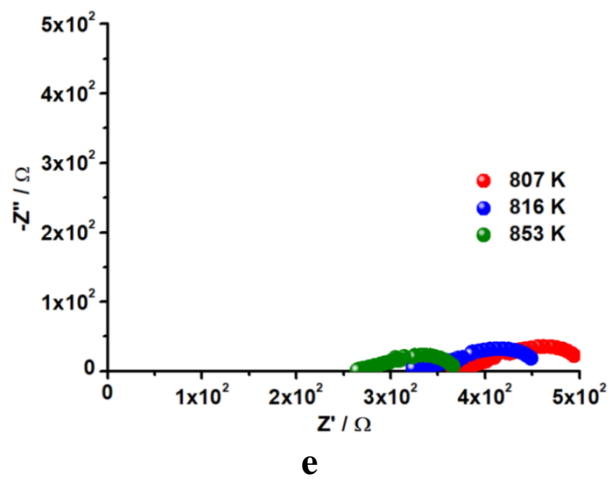


Figure 6.

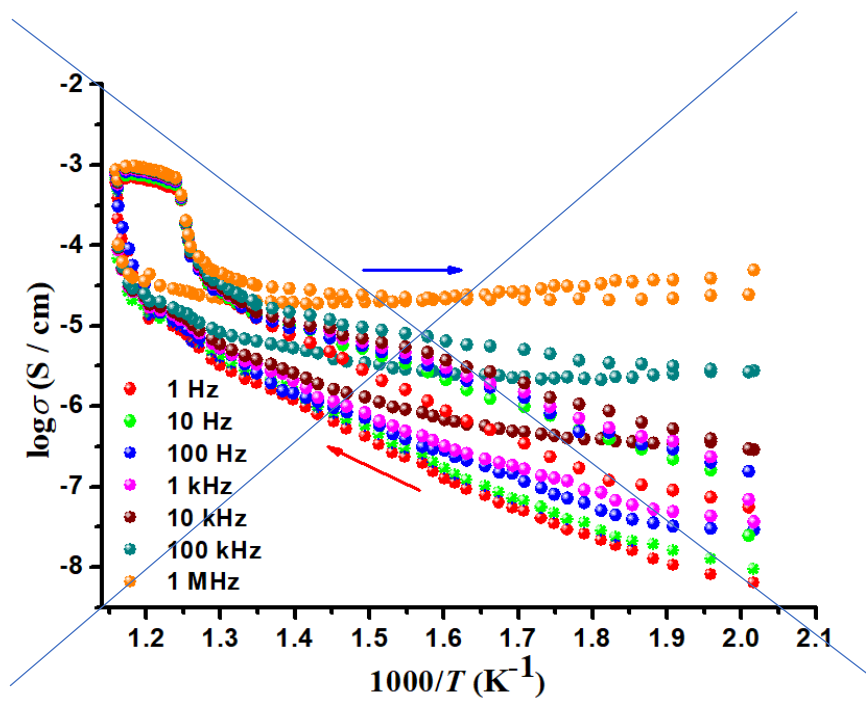


Figure 7.

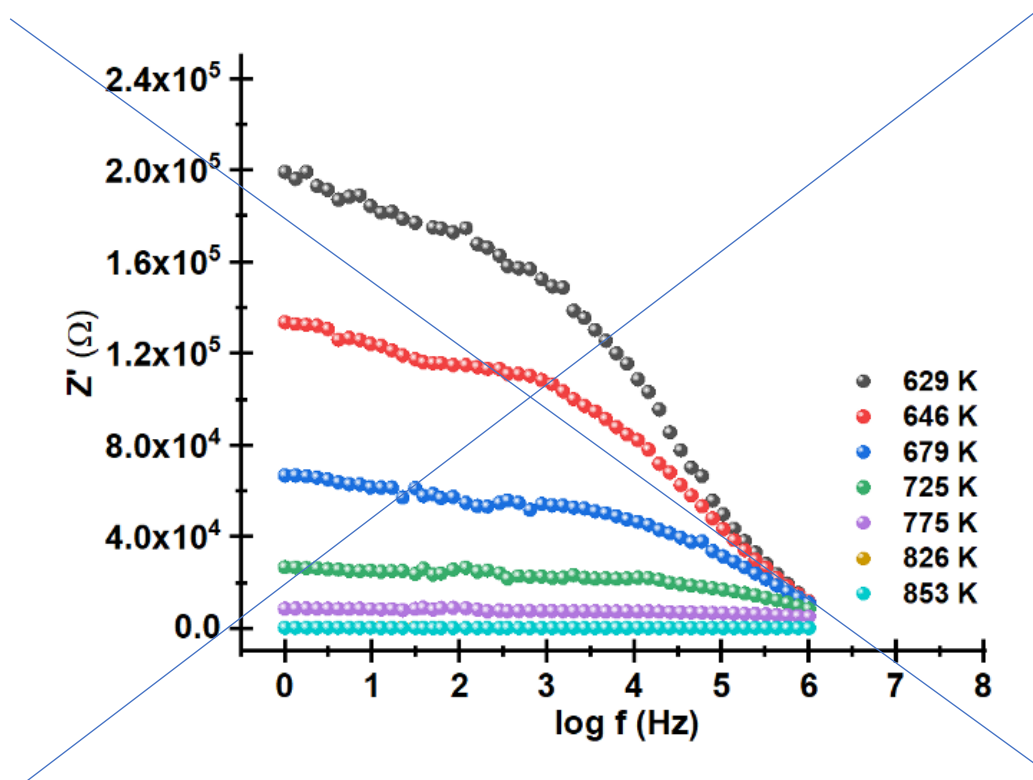


Figure 8.

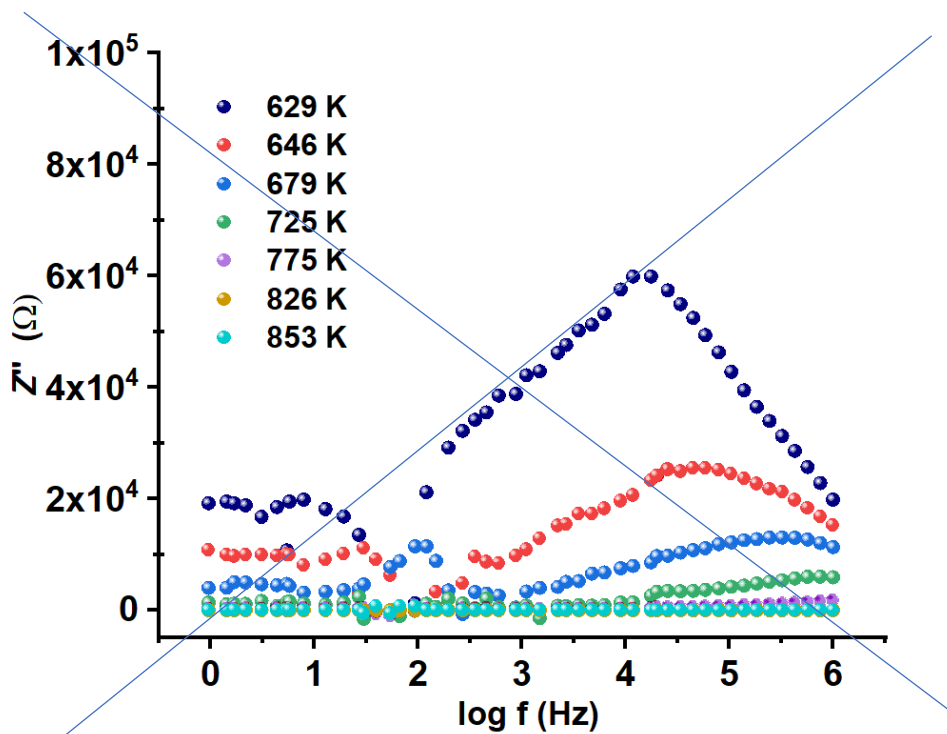


Figure 5.

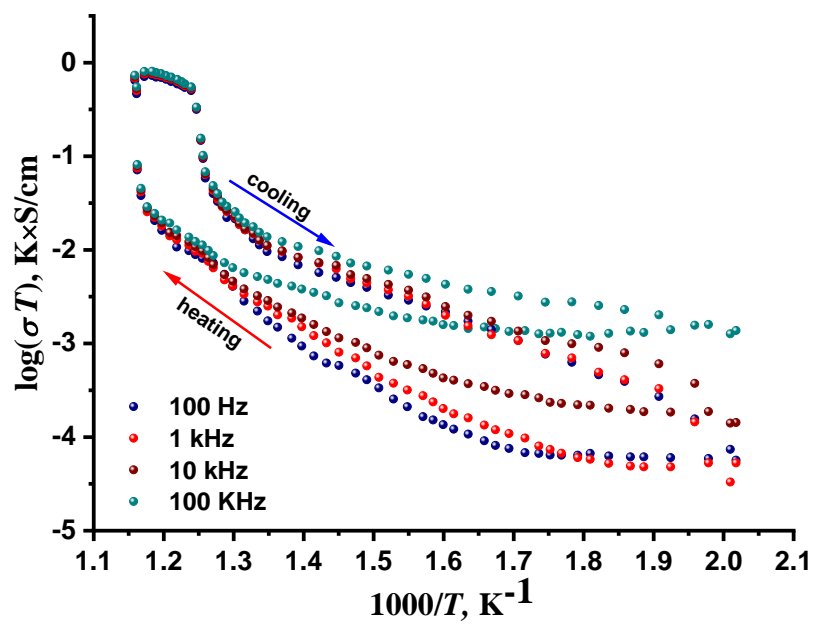


Figure 6.

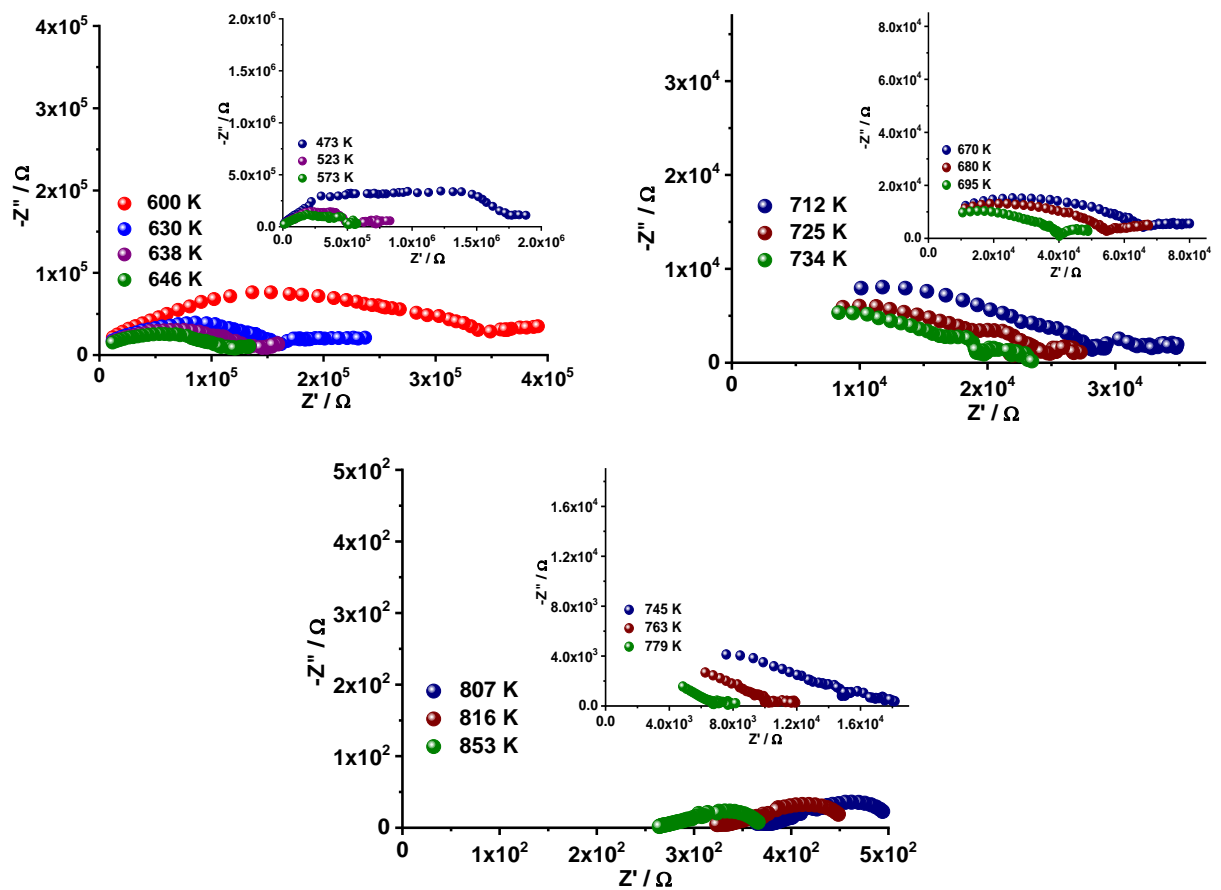


Figure 7.

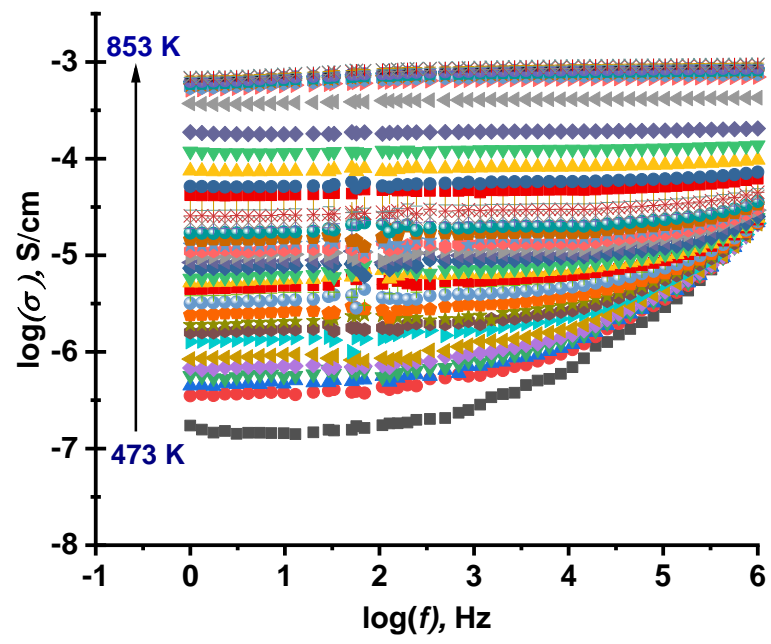


Figure 8.

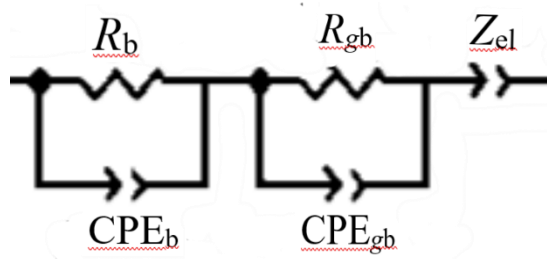


Figure 9.

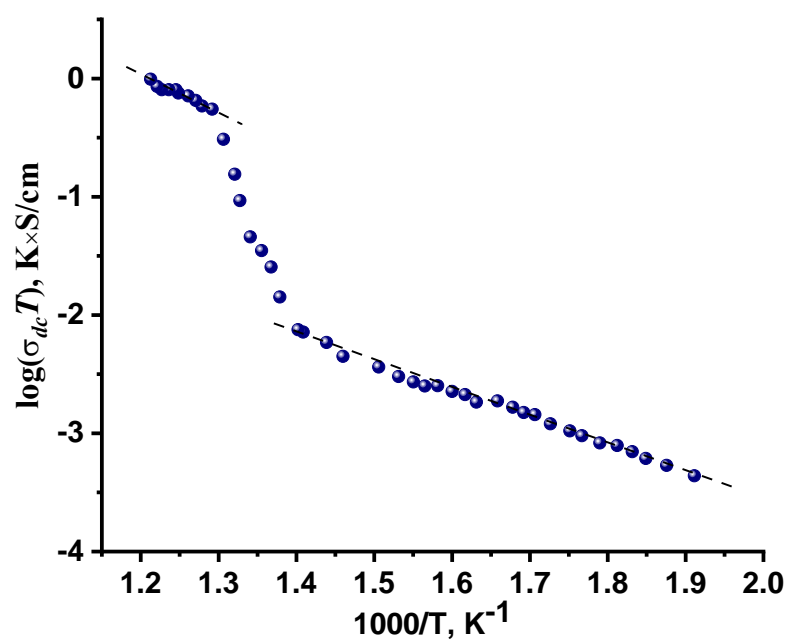


Table 1. Main parameters of processing and refinement of the $\text{Tl}_5\text{InHf}(\text{MoO}_4)_6$ sample

Compound	$\text{Tl}_5\text{InHf}(\text{MoO}_4)_6$
Sp.Gr.	$R\bar{3}c$
a , Å	10.63893 (5)
c , Å	38.1447 (3)
V , Å ³	3739.04 (4)
Z	2
2θ -interval, °	5-140
R_{wp} , %	4.59
R_p , %	4.70
R_{exp} , %	3.04
χ^2	1.51
R_B , %	3.10

Table 2. Fractional atomic coordinates and isotropic displacement parameters (\AA^2) of $\text{Tl}_5\text{InHf}(\text{MoO}_4)_6$

Atom	<i>x</i>	<i>y</i>	<i>z</i>	B_{iso}	<i>Occ.</i>
Mo	0.35048 (15)	0.05613 (14)	0.03328 (3)	1.54 (7)	1
Hf1	0	0	0	1.42 (9)	0.325 (12)
In1	0	0	0	1.42 (9)	0.675 (12)
Hf2	0	0	0.25	1.20 (8)	0.675 (12)
In2	0	0	0.25	1.20 (8)	0.325 (12)
Tl1	0	0	0.35503 (3)	3.28 (7)	1
Tl2	0.38767 (12)	0	0.25	4.14 (8)	1
O1	0.1699 (10)	0.0340 (11)	0.0320 (3)	1.95 (12)	1
O2	0.4828 (9)	0.2334 (10)	0.0493 (2)	1.95 (12)	1
O3	0.3549 (11)	-0.0789 (10)	0.0494 (3)	1.95 (12)	1
O4	0.4011 (10)	0.0507 (10)	-0.0061 (2)	1.95 (12)	1

Table 3. Main bond lengths (Å) of $\text{Tl}_5\text{InHf}(\text{MoO}_4)_6$

Mo—O1	1.816 (5)	Tl1—O3 ⁱⁱ	2.806 (9)
Mo—O2	1.805 (9)	Tl1—O4 ⁱ	2.980 (8)
Mo—O3	1.585 (9)	Tl2—O2 ⁱ	3.134 (6)
Mo—O4	1.607 (8)	Tl2—O3 ⁱⁱⁱ	3.103 (8)
(Hf1/In1)—O1	2.057 (10)	Tl2—O4 ⁱⁱ	3.037 (8)
(Hf2/In2)—O2 ⁱ	2.136 (9)		

Symmetry codes: (i) $-x+2/3, -y+1/3, -z+1/3$; (ii) $-x+y+2/3, -x+1/3, z+1/3$; (iii) $y+2/3, -x+y+1/3, -z+1/3$